INORGANIC CHEMISTRY FRONTIERS

RESEARCH ARTICLE

View Article Online
View Journal | View Issue

Cite this: *Inorg. Chem. Front.*, 2023, **10**, 3297

Lead-free hybrid indium perovskites with near-unity PLQY and white light emission using an Sb^{3+} doping strategy†

Ling-Kun Wu,[a] Ren-Fu Li,*[b] Wei-Yang Wen,[b] Qing-Hua Zou,[a]
Heng-Yun Ye[a,c] and Jian-Rong Li*[a,c]

Received 6th March 2023,
Accepted 24th April 2023

DOI: 10.1039/d3qi00420a

rsc.li/frontiers-inorganic

Low-dimensional hybrid organic–inorganic metal halides (OIMHs) have been extensively investigated for their structural tunability and unique optoelectronic properties. However, the synthesis of highly photoluminescent lead-free OIMHs remains challenging. To address this issue, we synthesized a series of hybrid OIMHs $(DETA)_3InCl_6{:}x Sb^{3+}$ (DETA = diethylenetriamine, x = 0–15%). With Sb^{3+} doping, the photoluminescence quantum yield (PLQY) is greatly improved from 4.84% to nearly 100%. Moreover, $(DETA)_3InCl_6{:}10\%Sb^{3+}$ single crystals exhibit strong yellow broadband emission originating from self-trapped exciton (STE) radiative recombination. Interestingly, when Sb^{3+} doping is 0.005%, the single crystal doped Sb emits white light at an excitation wavelength of 365 nm with CIE coordinates of (0.35, 0.36). We also explored the effect of Sb^{3+} dopants and STE state formation by DFT calculations and ultrafast transient absorption techniques. This research provides new insights into the design of high-performance photoluminescent materials based on hybrid metal halides.

1. Introduction

Luminescent materials are widely used in energy information, medical technology, sensors, and light-emitting diodes (LEDs).[1–3] In recent years, various types of luminescent materials, such as organic polymer emitters, metal complexes, rare earth oxide phosphors, and hybrid OIMHs,[4–7] have been extensively explored. Among them, organic–inorganic hybrid metal lead halide perovskites have become a strong competitor for various luminescent materials due to their excellent optoelectronic properties.[8–11] However, the inherent high toxicity of Pb^{2+} ions limits their practical application. Like Pb^{2+} ions, In^{3+} ions also possess a similar ionic radius, electronegativity, and ns^2 electron configuration. Specifically, indium-based compounds have low toxicity and better chemical stability in air, hence, they are regarded as a potential substitute for Pb^{2+}-based compounds.[12–14] Recently, Yue *et al.*[15] synthesized two zero-dimensional (0D) $[H_2EP]_2InCl_6{\cdot}Cl{\cdot}H_2O{\cdot}C_3OH_6$ and $[H_3AEP]InCl_6{\cdot}H_2O$, which exhibit blue emission (430 nm), and the highest PLQY of $[H_2EP]_2InCl_6{\cdot}Cl{\cdot}H_2O{\cdot}C_3OH_6$ is only 13.44%. Xia's group also reported 0D $(PMA)_3InBr_6$ [PMA^+: $(C_6H_5CH_2NH_3)^+$] indium-based hybrid halides, which exhibited strong broadband orange luminescence with a PLQY of about 35%.[16] Subsequently, Yuan *et al.*[17] reported 0D In-based OIMH $(C_{10}H_{22}N_2)_2In_2Br_{10}$ with high-efficiency intrinsic emission and a PLQY of up to 70%. Although relatively high PLQY pristine organic–inorganic indium halides have been reported, their PLQY is still not satisfactory. Doping with metal ions having ns^2 (Sb^{3+}, Te^{4+}, Bi^{3+}, and Sn^{2+}, *etc.*) electronic configurations has been proven to be an effective strategy for improving photophysical properties.[18–21] Sb^{3+} is an effective dopant used as a non-emitting system to activate photoluminescence (PL) emission due to the unique dynamic lone pair of electrons.[22,23]

It is possible to realize efficient luminescence by constructing a host–guest doping system, in which the inert host is doped with a luminescent species.[24] Designing a suitable host–guest system not only improves the photoluminescence efficiency[25] but can also adjust its energy bandgap and even realize the self-absorption effect of suspended aggregation.[26] However, the fabrication of an efficient luminescent host–guest system has to face the challenges ascribed to the even distribution of the guest ions in the host matrix. The use of larger organic cations to construct single-crystal bulk materials

---

[a] *Chaotic Matter Science Research Center, Faculty of Materials Metallurgy and Chemistry, Jiangxi University of Science and Technology, Ganzhou 341000, P. R. China. E-mail: jrli@fjirsm.ac.cn*
[b] *Fujian Institute of Research on the Structure of Matter, Chinese Academy of Sciences, Fuzhou, Fujian 350002, P. R. China. E-mail: lirenfu@fjirsm.ac.cn*
[c] *Jiangxi Provincial Key Laboratory of Functional Molecular Materials Chemistry, Jiangxi University of Science and Technology, Ganzhou 341000, P. R. China*

† Electronic supplementary information (ESI) available: Synthesis and characterization, including TGA, powdered XRD patterns, PL spectra, PLQY, EDS, XPS and crystallographic data of **$(DETA)InCl_6$** and **$(DETA)InCl_6{:}15\%Sb$**. CCDC 2243632 and 2243633. For ESI and crystallographic data in CIF or other electronic formats see DOI: **https://doi.org/10.1039/d3qi00420a**

with 0D structures is an effective way to obtain suitable host–guest systems.[27–30] This is because larger organic cations make it easier for luminescent substances to be regularly embedded in the host matrix without causing the formation of electronic bands. As the dimensions vary from 3D, 2D to 1D and 0D, the strong electron–phonon coupling increases, leading to the formation of commonly recognized self-trapping excitons (STEs).[10,31,32] In particular, the formation of self-trapped exciton (STE) states in the 0D structure with isolated polyhedra is closely related to structural distortion and dielectric confinement effects, which is one of the reasons for the higher PLQY of 0D metal halides.[33,34] In addition, the formation of STEs results in an emission spectrum covering the entire visible spectrum. The combination of STEs and free excitons (FEs) can easily lead to dual emission bands, which are favorable conditions for the formation of white light emission.[35–37] Recently, a large number of white-emitting lead-based hybrid perovskites, such as 2D perovskite (2meptH$_2$)PbCl$_x$Br$_{4-x}$(2mept = 2-methyl-1,5-diaminopentane, x = 0–4),[38] 1D hybrid perovskite TMGPbX$_3$ (TMG = 1,1,3,3-tetramethylguanidine, X = Cl$^-$, Br$^-$ or I$^-$)[39] and 0D (TAE)$_2$[Pb$_2$Cl$_{10}$](Cl)$_2$(TAE = tris(2aminoethyl)ammonium(C$_6$N$_4$H$_{22}$))[40] single crystals, have been reported. These hybrid lead-based halides all exhibit excellent optical properties and double emission bands resulting from the broadband yellow-green emission induced by STEs and the narrow blue emission spectrum assisted by FE. Unfortunately, most of them are lead-based hybrid perovskites mentioned above. These bring about the necessity of developing cost-effective, environmentally friendly and high PLQY luminescent materials.

Using the crystal engineering strategy, we synthesized a series of new 0D hybrid OIMH single crystals (DETA)InCl$_6$:x% Sb^{3+} (x = 0–15%). (DETA)InCl$_6$:10%Sb^{3+} exhibits broadband yellow emission with a peak at 571 nm, and a PLQY of ~100% was obtained when excited at 342 nm wavelength. Interestingly, dual-band visible white emission was obtained by doping 0.005% Sb^{3+} in the (DETA)InCl$_6$ lattice, and the CIE coordinates at an excitation wavelength of 365 nm were (0.35, 0.36), respectively. Detailed analysis of the photophysical mechanism using DFT and femtosecond transient absorption (fs-TA) spectroscopy reveals that the broadband emission originates from triplet state emission-generated STEs and strong exciton–phonon coupling. Finally, a pumped white light-emitting diode (WLED) based on (DETA)InCl$_6$:10%Sb^{3+} was prepared, demonstrating that the compound has a promising application in solid-state lighting.

2. Results and discussion

2.1 Crystal structures and supramolecular interactions

Single crystal X-ray analysis revealed that the compound (DETA)InCl$_6$ crystallizes in the monoclinic space group $I2/a$. The unit cell parameters are a = 13.2661(4) Å, b = 10.0585(5) Å, c = 28.4784(8) Å, β = 90.496(3), V = 2858.31(14) Å^3, Z = 8 (Table S2†). As shown in Fig. 1a, the asymmetric unit of the (DETA)InCl$_6$ single crystal consists of one [DETA]$^+$ cation and two and a half [InCl$_6$]$^{3-}$ anions.

In the [InCl$_6$]$^{3-}$ octahedron, the In–Cl bond lengths range between 2.485 and 2.542 Å, and the Cl–In–Cl bond angles range from 87.33 to 92.29° (Fig. 1b and Table S3†). This means that the [InCl$_6$] octahedron is easily distorted, and the degree of distortion of the inorganic polyhedra in 0D OIMHs is closely related to STEs.[41] The degree of deformation of the pristine [InCl$_6$]$^{3-}$ octahedron and the [InCl$_6$]$^{3-}$ octahedron doped with 15% Sb can be calculated using eqn (1) and (2):[42]

$$\Delta d = \tfrac{1}{6}\sum_{n=1}^{6}\left[\frac{d_n - d}{d}\right]^2 \tag{1}$$

$$\sigma^2 = \tfrac{1}{11}\sum_{n=1}^{12}\left[\theta_n - 90^\circ\right]^2 \tag{2}$$

where Δd is the variance of the bond length of In–Cl and σ^2 is the variance of the bond angle of Cl–In–Cl. These two parameters are usually used to evaluate the degree of polyhedron distortion. d_n, d, and θ_n are the individual bond length of In–Cl, the average bond length of In–Cl, and the bond angle of Cl–In–Cl, respectively. The octahedral distortions are Δd = 0.863 × 10^{-4} and σ^2 = 2.576 for (DETA)InCl$_6$ and Δd = 1.224 × 10^{-4} and σ^2 = 5.719 for (DETA)InCl$_6$:15%Sb^{3+}, respectively. From the data, we found that the Sb^{3+} doped [InCl$_6$]$^{3-}$ octahedron has a greater degree of deformation. Such octahedral distortions are comparable to the recently reported In-based OIMHs,[43] but lower than the general Pb, Sn, and Sb-based OIMH compounds, which is due to the existence of s orbitals to generate strong antibonding highest occupied orbitals.[40] Notably, supramolecular interactions such as hydrogen bonding are ubiquitous in hybrid metal halides. Therefore, we further analyzed the hydrogen bond between the inorganic anion [InCl$_6$]$^{3-}$ and the organic cation [DETA]$^{3+}$; the hydrogen bonding details are presented in Table S4.† As shown in Fig. 1a, each inorganic component [InCl$_6$]$^{3-}$ is connected to organic cations through three N–H⋯Cl. The distance of H⋯Cl ranges from 2.38(3) Å to 2.633(8) Å, D⋯A distances range from 3.109(9) Å to 3.279(8) Å and D–H⋯A angles range from 129.45 (15) to 172(6)°. Based on previous studies,[17] we found that the emission efficiency of 0D metal halides is affected by the concentration of luminescent active centers, that is, the distance between adjacent [InCl$_6$]$^{3-}$ anions. From Fig. S1,† we observed that the distance between In⋯In along the b-axis ranges from 7.636 to 8.161 Å, which is slightly lower than that of previously reported In-based OIMHs.[15] At the same time, it also shows that the electronic coupling interaction between [InCl$_6$]$^{3-}$ anions is weak, which can inhibit non-radiative energy transfer and promote radiative recombination.[44,45] To explore the thermal stability of single crystals, we performed thermogravimetric analysis (TGA) and found that the mass loss of (DETA)InCl$_6$ occurred at 213 °C (Fig. S2†), showing that the compound has great thermal stability below 200 °C. In general, In-based OIMHs can easily crystallize with water or organic solvent molecules, which causes the structures to collapse upon losing their solvent molecules at lower

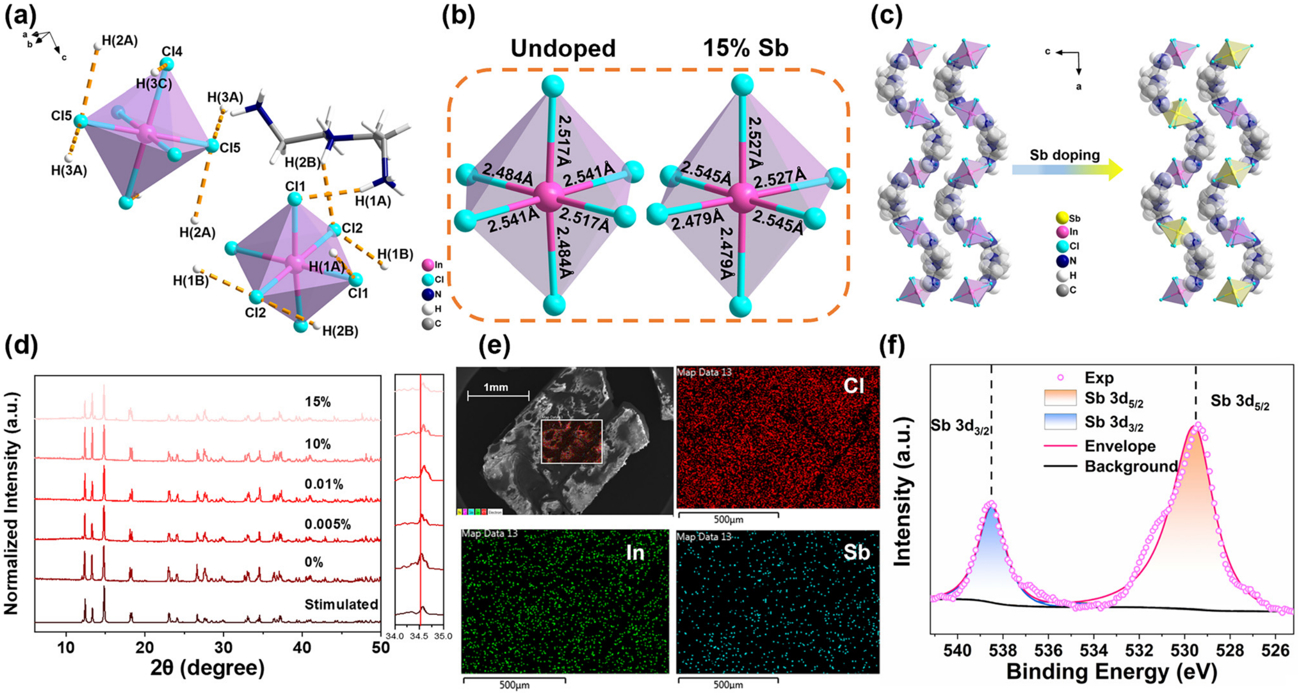

Fig. 1 (a) The asymmetric unit of compound (DETA)$InCl_6$ (the yellow dotted line represents the N–H⋯Cl hydrogen bond). (b) Details of the octahedral bond lengths of undoped and doped 15% Sb. (c) Structural stacking diagram of Sb^{3+} doped (DETA)$InCl_6$ single crystals. (d) PXRD patterns of the pristine and Sb^{3+} doped (DETA)$InCl_6$. (e) Energy dispersive X-ray spectroscopy (EDS) mapping images of In, Sb, and Cl elements in the (DETA)$InCl_6$:15%Sb^{3+} single crystal. (f) XPS spectrum of Sb in (DETA)$InCl_6$:Sb^{3+}.

temperatures.[14,46] In comparison, (DETA)$InCl_6$ has the advantage of good thermal stability.

Metal doping strategies are usually effective ways to change the emission band and improve the quantum efficiency. We obtained the (DETA)$InCl_6$:$x$$Sb^{3+}$ (x = 0.005%, 0.01%, 10%, 15%) single crystal. From Fig. 1c, we can observe that when Sb^{3+} is doped into (DETA)$InCl_6$ and the position of In^{3+} ions is occupied by Sb^{3+} ions, but the configuration does not change. From the PXRD pattern with different ratios of (DETA)$InCl_6$:$x$$Sb^{3+}$ (Fig. 1d), we can clearly observe that the curves are basically consistent except for a slight shift in the diffraction peaks, indicating that the samples are pure phase. This slight shift of the diffraction peaks is attributed to the fact that the ionic radius of In^{3+} is larger than that of Sb^{3+}. As shown in Fig. 1e, energy dispersive spectroscopy (EDS) shows that In, Cl, and Sb elements of the (DETA)$InCl_6$:15%Sb^{3+} single crystal are uniformly distributed, well overlapped with the SEM image signal, and the formation of impure phases is ruled out. The elemental analysis obtained from EDX shows that In : Sb corresponds to 3.54 : 0.54 (Fig. S3†), basically, consistent with the actual doping amount. To directly demonstrate the successful doping of Sb^{3+}, we performed X-ray electron spectroscopy (XPS) on (DETA)$InCl_6$:15%Sb^{3+}. The sample exhibited XPS peaks of In, Cl, and Sb (Fig. S4†), where Fig. 1f shows that the peaks at 538.5 and 529.5 eV are attributed to the $3d_{3/2}$ and $3d_{5/2}$ signals of Sb^{3+}, respectively. To prove the presence of Sb^{3+} (DETA)$InCl_6$ crystals, chemical analyses of the as-prepared samples were performed using the ICP-MS technique. The final molar ratios of the Sb^{3+} dopant concentration in the (DETA)$InCl_6$ crystal were all close to the initial ones (Table S1†).

2.2 Optical properties

Fig. 2a shows the photoluminescence excitation (PLE) and PL spectra of (DETA)$InCl_6$:$x$$Sb^{3+}$ (x = 0%, 0.005%, 0.01%, 0.1%, 0.15%). When x = 0, the compound exhibits obvious bimodal emission at an excitation wavelength of 325 nm, high-energy short-wave blue emission at 400 nm, and low-energy yellow emission at 575 nm. We speculated that the high-energy short-wave emission at 400 nm was derived from $[DETA]^{3+}$, and recorded the PL spectrum of (DETA)Cl_3 (Fig. S5†). We found that the maximum emission peak of (DETA)Cl_3 is also located at 400 nm, which basically coincides with the maximum peak of the spectrum of $(DETA)_3InCl_6$, indicating the reliability of our speculation. Moreover, we found that when a small amount of Sb^{3+} was added, the double-peak emission disappeared, and the emission spectrum showed broad-band yellow emission. We can also intuitively observe that the intensity of the excitation peak reaches its maximum when the doping amount is 10%, which is consistent with the PLQY results presented in Fig. 3b. To further show that doping leads to the change in the luminescence colour, in Fig. S6,† the images of (DETA)$InCl_6$:$x$$Sb^{3+}$ crystals with different proportions of Sb at the excitation wavelength of 365 nm under the irradiation of a daylight lamp and an ultraviolet lamp are presented. The energy levels of this ns^2 electronic configuration of

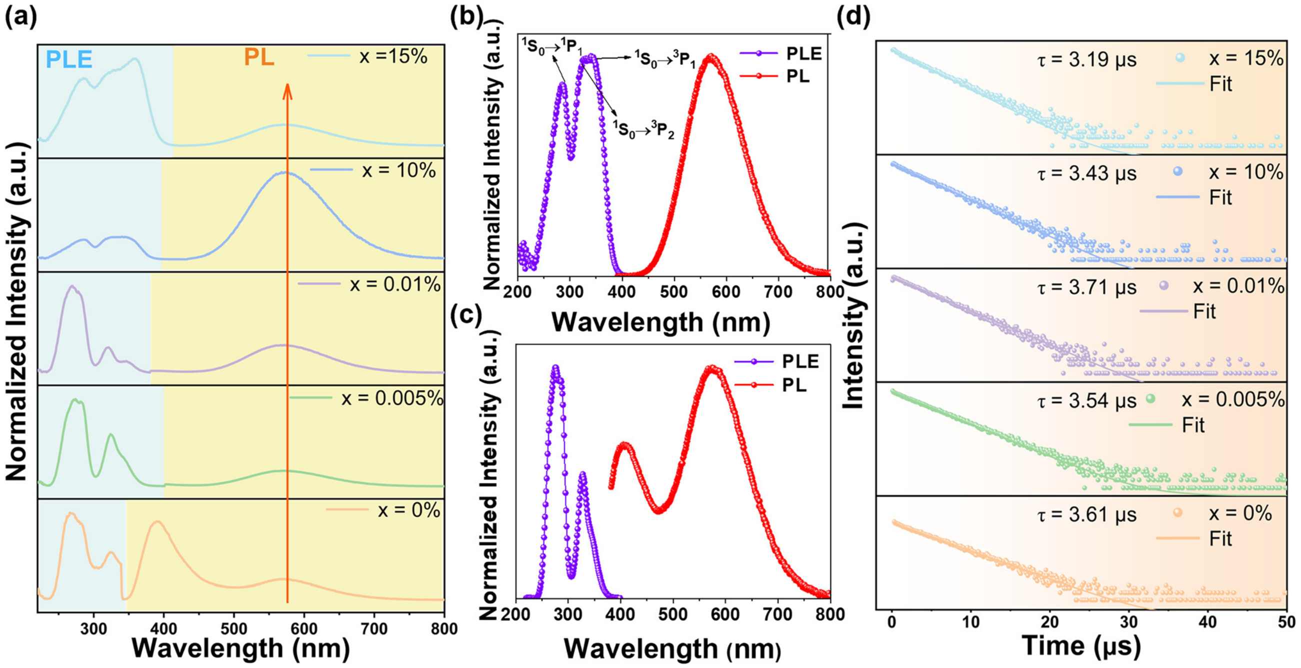

Fig. 2 (a) Normalized PLE and PL spectra of (DETA)InCl$_6$:*x*Sb^{3+} (*x* = 0%, 0.005%, 0.01%, 10%, 15%). (b) PLE and PL spectra of (DETA)InCl$_6$:10%Sb^{3+}. (c) PLE and PL spectra of (DETA)InCl$_6$: 0.005%Sb^{3+} excited at 365 nm. (d) Lifetime decay curves of (DETA)InCl$_6$:*x*Sb^{3+} with different contents.

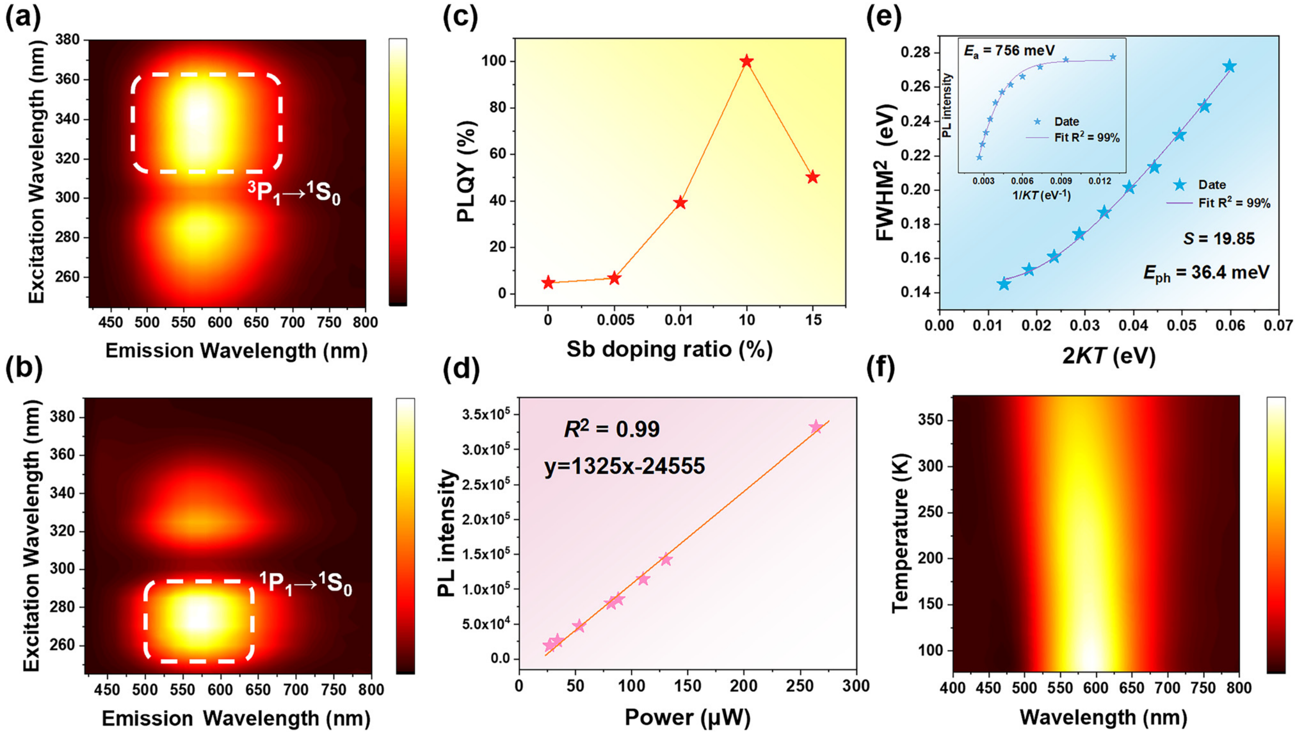

Fig. 3 (a and b) Cloud images of (DETA)InCl$_6$:10%Sb^{3+} and (DETA)InCl$_6$:0.005%Sb^{3+} measured at different emission wavelengths. (c) PLQY line diagram of (DETA)InCl$_6$:*x*Sb^{3+} doped with different Sb ratios. (d) (DETA)InCl$_6$:10%Sb^{3+} excitation power dependent PL spectrum. (e) Fitting results of FWHM^2 as a function of temperature (the inset is the fitting curve of 1/*KT* and PL intensity). (f) (DETA)InCl$_6$:10%Sb^{3+} contour plots of the temperature as a function of wavelength.

Sb^{3+} have been widely reported, namely the excited singlet state $^1P_1$ and the triplet state $3P_n$ (n = 0, 1, 2), and the ground state $^1S_0$.[47,48] From the perspective of transition rules, the transition from the ground state $^1S_0$ to the excited state $^1P_1$ is ascribed to the spin–orbit coupling effect, while part of the ground state $^1S_0$ to the triplet state $^3P_1$ transition requires lattice vibration and spin–orbit interaction. However, in general, the transitions from $^1S_0$ to the triplet states $^3P_2$ and $^3P_0$ are forbidden, but their transitions can be assisted by lattice vibrations.[49,50] Fig. 2b shows the excitation and emission spectra of (DETA)$InCl_6$:10%Sb^{3+}. The peak at 290 nm in the excitation spectrum is called the C-band ($^1S_0 \rightarrow {}^1P_1$), and the peak near 325 nm is the B-band ($^1S_0 \rightarrow {}^3P_2$). From the perspective of the PLE spectrum, the best excitation band is the A band at 342 nm ($^1S_0 \rightarrow {}^3P_1$). The PL spectrum obtained with the best excitation band has a maximum peak at 571 nm, and the compound exhibits broadband emission. It can be seen that the Stokes shift is as high as 229 nm and the full width at half maximum (FWHM) is 132 nm. Fig. 2c shows the PLE and PL spectra of (DETA)$InCl_6$:0.005%Sb^{3+}. It can be clearly seen that there is significant doublet emission under excitation at 370 nm, with peaks at 446 nm and 570 nm, respectively. Compared with the previously reported doublet of cuprous OIMH $[(C_3H_7)_4N]_2Cu_2I_4$, the doublet emission peak is significantly narrower. Its peak 1 is located at 483 nm and peak 2 is located at 637 nm. The dual-emission band separation (154 nm) is higher than (DETA) $InCl_6$:0.005%Sb^{3+} (124 nm).[51] We attribute the excitation peak at 446 nm to the emission of the In component and the peak at 570 nm to the emission of the Sb component; both emission peaks are due to the independent ns^2 metal centers (In^{3+} and Sb^{3+}), which are common in 0D OIHMs. Fig. S7† shows the CIE coordinate diagram of (DETA) $InCl_6$:0.005%Sb^{3+} under different excitation bands, and what is exciting is that the coordinate values (0.35, 0.36) at 365 nm are very close to the standard white light. Except for the pristine (DETA)$InCl_6$, which is fitted with a double exponential function, the others are fitted with a single exponential function $I(t) = A\exp(-t/\tau)$. In addition, we also found that the photoluminescence lifetime significantly increased after doping Sb^{3+}, in the range of 3.19–3.71 μs, which is comparable to that of previously reported Sb-based 0D OIMHs.[52]

To deeply investigate the luminescence mechanism, we explored the wavelength-dependent PLE and PL spectra at doping levels of 10% and 0.005% Sb. As shown in Fig. 3a, b and S8,† the PL spectrum of the Sb^{3+} ion is easily affected by the magnitude of the excitation energy, which has a great influence on the excitation and recombination rate. The origin of yellow broadband emission is explained by testing the dependent emission spectrum within a wavelength range of 255–380 nm. From Fig. S8,† we can see that the launching peak has almost no offset, which confirms that the Sb^{3+} ion doping is not a combination of multiple excited state levels. From the cloud image of the excitation-related emission spectrum with a doping amount of 10%, we can also find an obvious emission peak at 570 nm. The peak intensity of the excitation band is obviously concentrated in the above-mentioned optimal band ($^3P_1 \rightarrow {}^1S_0$), while the excitation peak intensity of doping with 0.005% is concentrated in the C band ($^1P_1 \rightarrow {}^1S_0$), and a small part is located in the A and B bands. These conclusions correspond to Fig. 2b and c. Fig. 3b shows the PLQY line graph of (DETA)$InCl_6$ doped with different proportions of Sb^{3+}. As the doping amount increases, the PLQY increases until the doping amount is 10%, and the PLQY is nearly 100% (Fig. S9†). The PLQY dropped sharply when Sb^{3+} was continued to be doped. The energy migration between Sb^{3+} ions and surface defects are the main reasons for the decrease of PLQY. In order to rule out broadband emission caused by permanent trap states, we tested the excitation power *versus* the PL intensity map (Fig. 3d). We found that the PL intensity increases with the increase of the excitation power, satisfying a good linear function relationship. Generally speaking, the emission characteristic of the permanent trap state is that the PL intensity reaches saturation when the excitation power increases. So we further demonstrate that the emission mechanism is not a permanent trap state.[53]

To further explore the photophysical mechanism and electron–phonon coupling effects, we recorded the temperature-dependent PL spectra. Fig. S10† shows the temperature-dependent PL spectra of (DETA)$InCl_6$:10%Sb^{3+} in the temperature range of 77–377 K at an excitation wavelength of 342 nm. We found that the PL intensity decreased with increasing temperature. This phenomenon can be explained by the fact that non-radiative recombination is easily suppressed at low temperatures. The higher temperature results in a greater possibility of non-radiative transition, which may be due to the increase of phonon state occupation and the increase of electron–phonon coupling at high temperatures.[54] It is worth noting that the PL emission spectrum undergoes a red shift as the temperature decreases. This has also been found in other low-dimensional light-emitting halogenated materials based on STEs, because the thermal expansion of the lattice caused by the increase in temperature leads to a distortion of the lattice and a reduction of the band gap.[55,56] Of course, it may also be the dominant effect of electronic coupling. The CIE coordinates shown in Fig. S10† range from (0.44, 0.49) to (0.50, 0.48), which more intuitively reflects the redshift phenomenon. Furthermore, the Huang–Rhys factor (S) and the exciton activation energy (E_a) are important parameters used to understand the underlying photophysical mechanism. In the formation of STEs, strong electron–phonon coupling is particularly important, and S is usually used as an evaluation criterion (Fig. 3e). S can be obtained by fitting the direct relationship between the FWHM and the temperature (eqn (3)).[57]

$$\mathrm{FWHM} = 2.36\sqrt{S}\hbar\omega_{\mathrm{photon}}\sqrt{\coth\frac{\hbar\omega_{\mathrm{photon}}}{2K_bT}} \tag{3}$$

where K_b is Boltzmann's constant, $\hbar\omega_{\mathrm{photon}}$ is the optical phonon frequency, after calculation, S is 19.85, and $\hbar\omega_{\mathrm{photon}}$ is 36.4 meV. Among them, S is significantly larger than the ordinary quantum dots (ZnSe ~ 1) used before. Such a large S in the compound also marks a strong electron–phonon coupling, which makes STEs easy to form. E_a can be obtained using Arrhenius equation (4):[58]

$$I(T)=\frac{I_0}{1+Ae^{-\frac{E_a}{K_b T}}} \tag{4}$$

where I_0 is the PL intensity at 0 K; we can obtain E_a as 756 meV as shown in the inset of Fig. 3e, which is much larger than the thermal energy at room temperature. It is also larger than the previously reported 0D OIMHs $(H_3AEP)_2CdBr_6{\cdot}2Br$ (154.81 meV)[59] and $(C_4H_{14}N_2)_2In_2Br_{10}$ (61.8 meV).[60] This indicates the excellent thermal stability of this compound, and the highly localized STE is usually fed back by a large E_a. The false-color map of Fig. 4f provides direct evidence for the large broadband emission and also confirms that the quenching temperature of PL reaches at least 350 K. In brief, all the above conclusions suggest that the large broadband emission, the Stokes shift, S and E_a result from the strong Jahn–Teller distortion.

2.3 Electronic band structure calculation

To further elucidate the photophysical properties of (DETA)$InCl_6$ and (DETA)$InCl_6$:Sb^{3+} in detail, electronic band structures and density-of-state maps were obtained using DFT calculations. Fig. 4a shows that the highest occupied molecular orbital (HUMO) and the lowest occupied molecular orbital (LUMO) of (DETA)$InCl_6$ are both at the G point, so it can be judged that (DETA)$InCl_6$ has a direct band gap with a value of 3.97 eV. (DETA)$InCl_6$:15%Sb^{3+} has an indirect band gap with a value of 2.76 eV (Fig. 4b), and while the LUMO is still at the G point, the HUMO moves to the Q point in the momentum space. This shift in bandgap properties is attributed to the fact that the Sb-5s orbitals constitute the inner gap band (located above the pristine HUMO). The valence band maximum (VBM) of undoped (DETA)$InCl_6$ mainly consists of organic components, In-4d and Cl-3p orbitals. The composition of the VBM of (DETA)$InCl_6$:15%Sb^{3+} is basically consistent with the pristine compound, but with increased Sb-5s and Sb-5p orbital contributions. And we found that the conduction band minimum (CBM) of (DETA)$InCl_6$:15%Sb^{3+} was contributed by inorganic components (In-5s, Sb-5p). Based on the above analysis, it can be directly demonstrated that the PL emission mechanism is influenced by the doping sites in the inorganic part, resulting in broadband yellow emission. It is a common phenomenon that the DFT calculation values are lower than the experimental values.[61] In our case, the calculated values of the above bandgaps are significantly lower than the experimental values of 4.77 eV and 3.23 eV (Fig. 4e and f).

The femtosecond transient absorption (fs-TA) technique has been employed to study ultrafast photophysical processes. The ultrafast charge carrier dynamics were obtained by the fs-TA technique for (DETA)$InCl_6$:0.005%Sb^{3+} and (DETA)

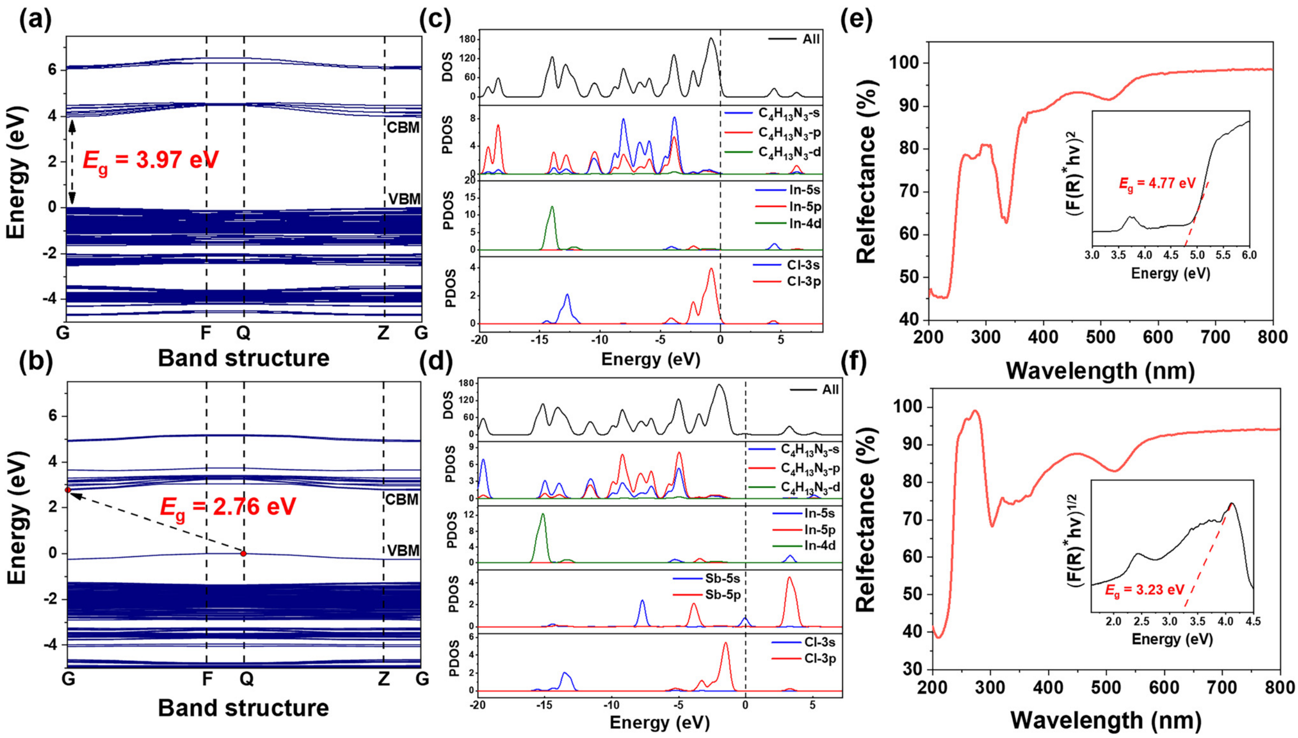

Fig. 4 Band structures of (DETA)$InCl_6$ (a) and (DETA)$InCl_6$:15%Sb^{3+} calculated by DFT-PBE (b). (c and d) Total density of states and the partial density of states of (DETA)$InCl_6$ and (DETA)$InCl_6$:15%Sb^{3+} based on the DFT-PBE method. (e and f) DRS spectra of (DETA)$InCl_6$ and (DETA)$InCl_6$:Sb^{3+} at room temperature.

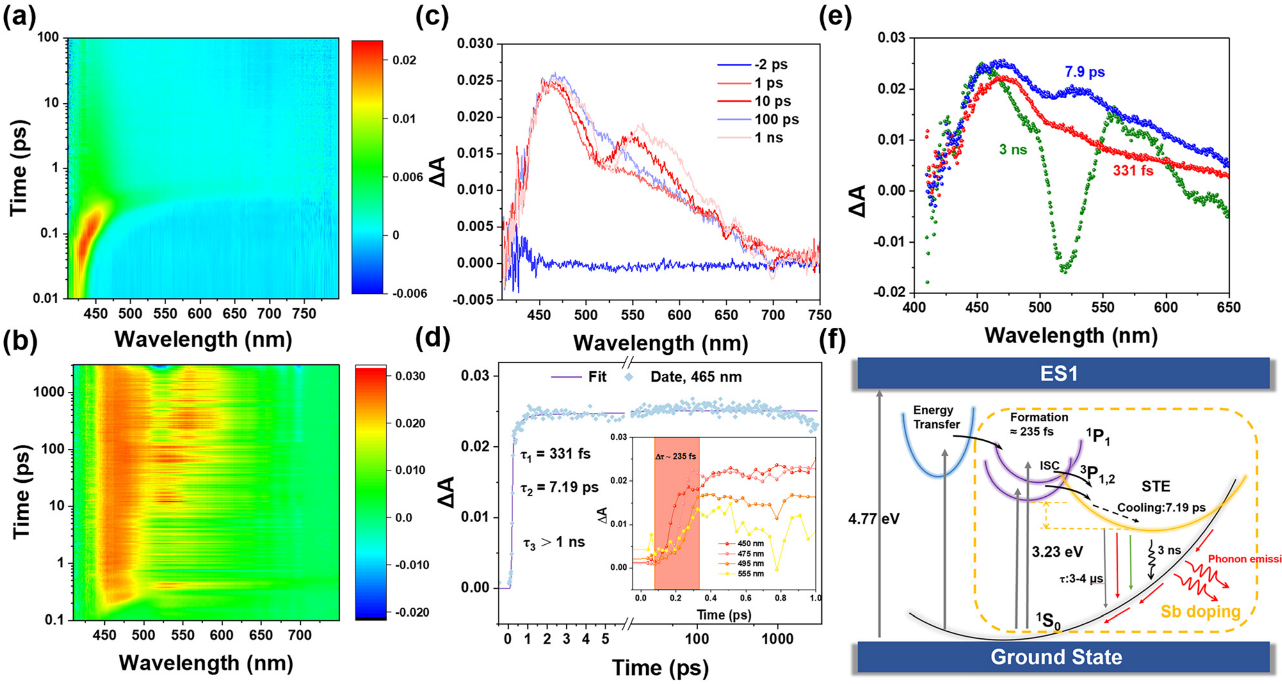

Fig. 5 (a and b) False-color TA images of (DETA)$InCl_6$:0.005%Sb^{3+} and (DETA)$InCl_6$:10%Sb^{3+} single crystals. (c) fs-TA spectrum of (DETA)$InCl_6$:10% Sb^{3+}. (d) PIA attenuation signals of (DETA)$InCl_6$:10%Sb^{3+} (the inset shows the detection of PIA at different wavelengths). (e) (DETA)$InCl_6$:10%Sb^{3+} single crystal fs-TA signal dynamics. (f) Schematic diagram of the photophysical mechanism of (DETA)$InCl_6$:10%Sb^{3+}.

$InCl_6$:10%Sb^{3+} to demonstrate and observe the formation of STEs. As shown in Fig. 5a, the broad pump-induced absorption (PIA) signal of the entire spectrum can be observed substantially at the excitation wavelength of 365 nm, demonstrating the broad white light emission. Extensive positive PIA was observed in the probe region (450–590 nm), demonstrating that the STEs lead to broadband yellow PL emission (Fig. 5b). We also tested the attenuation curves of PIA signals at different wavelengths and found that their motion trajectories were basically the same (Fig. S11†), which also satisfied the characteristics of STEs. It can be observed in Fig. 5c that ΔA decreases with increasing wavelength, but the overall trend of ΔA corresponds to the false colour map shown in Fig. 5b. The PIA decay signal for (DETA)$InCl_6$:10%Sb^{3+} can be fitted with a triple exponential function to obtain the following three components, τ_1 = 330.5 fs, τ_2 = 7.19 ps, and τ_3 > 1 ns (Fig. 5d). According to previous reports,[62] such a fast component of τ_1 indicates that the contribution of triplet TA to PIA may be negligible because the intersystem transit time from spin singlet STEs to spin triplet STEs is usually on the order of picoseconds. The τ_2 component is due to the cooling of the hot STE state.[63] The slow component of τ_3 is beyond the time window and will not be discussed in detail here. It is worth noting that the inset of Fig. 5d shows the synchronous generation of STEs at different wavelengths, because they have almost the same PIA rise time (~235 fs), indicating that there is almost no potential barrier between free excitons and STEs. Of course, we also provide a global fit to analyze the TA dynamics of the three components (Fig. 5e). Combining all the above fluorescence spectral characterization studies, DFT calculations, and fs-TA analysis the overall STEs are shown in Fig. 5f.

2.4 Preparation of WLEDs

The stability of (DETA)$InCl_6$:10%Sb^{3+} phosphor powder was recorded by PXRD. The powder diffraction peaks of the sample stored for three months were almost the same as those of the fresh sample (Fig. S12†). In addition, we also tested the PL intensity stability of (DETA)$InCl_6$:10%Sb^{3+}. We found only a slight decrease in the PL intensity of the compound over 7 days, Fig. S13.† Such excellent stability and optical properties facilitate the construction of WLED devices. Fig. 6a is a conceptual diagram of the prepared LED device. The mixture of the metal halide (DETA) $InCl_6$:10%Sb^{3+} and $BaMgAl_{10}O_{17}$:Eu^{2+} was stirred to form a colloidal mixture. Then the mixture was kept under an LED lampshade to cure for 1 hour and finally the UV lamp chip was covered. Because the excitation of the above two phosphors is in the ultraviolet region, a 365 nm ultraviolet LED was selected as the pumping light source. Fig. 6b shows the actual image of the LED and the image after current driving. The fabricated WLED exhibited white emission due to the driving current (Fig. 6c). The correlated colour temperature and the colour rendering index are 6927 K and 91.2, respectively. The CIE coordinates of the device are (0.30, 0.31). We also recorded the PL spectra under different driving currents, and the luminous intensity of WLEDs increased with the increase of driving current, proving the application prospects of this device in high-power devices (Fig. S14†).

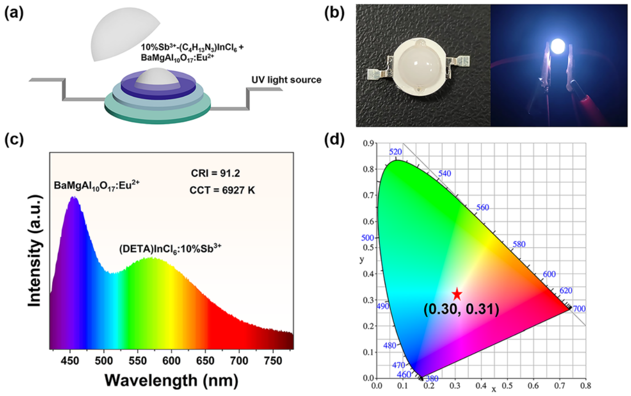

Fig. 6 (a) Conceptual diagram of the prepared LED device. (b) WLED-powered and not powered images. (c) Emission spectra of WLED devices made of (DETA)$InCl_6$:10%Sb^{3+}. (d) CIE coordinates of WLED devices.

3. Conclusion

In summary, we synthesized a series of novel 0D hybrid OIMH single crystals (DETA)$InCl_6$:x%Sb^{3+} (x = 0–15%). When Sb^{3+} ions were introduced into (DETA) $InCl_6$, it was found that the original emission band changed from cyan emission to yellow broadband emission. Excitingly, ~100% PLQY was achieved when the doping amount was 10% Sb. The detailed PL and PLE spectra and fluorescence lifetime spectra show a Stokes shift of 229 nm and a long fluorescence lifetime of 3.19–3.71 μs, all indicating that it exhibits intrinsic STE emission behaviour. Then we found that when the doping amount is 0.005% Sb^{3+}, the compound can change the emission band with the change of the excitation band. White light emission was realized at the excitation wavelength of 365 nm, and its CIE coordinates were (0.35, 0.36), which are very close to the standard white light. DFT calculations confirmed that doping Sb^{3+} ions can effectively modulate the photophysical properties of (DETA)$InCl_6$. The ultrafast charge carrier dynamics and the formation of STEs were studied in detail using the fs-TA technique. In view of the excellent optoelectronic properties of this series of compounds, we fabricated WLEDs based on (DETA) $InCl_6$:10%Sb^{3+}. This report provides an effective strategy for the development of highly efficient photoluminescent materials.

Author contributions

Ling-Kun Wu: methodology, validation, data curation, formal analysis, investigation, and writing – original draft. Ren-Fu Li: writing – review & editing, validation, and data curation. Wei-Yang Wen: data curation. Qing-Hua Zou: data curation. Heng-Yun Ye: funding acquisition and supervision. Jian-Rong Li: writing – original draft, formal analysis, investigation, data curation, visualization, writing – review & editing, and funding acquisition.

Conflicts of interest

There are no conflicts to declare.

Acknowledgements

This work was supported by the National Natural Science Foundation of China (22275075), the Natural Science Foundation of Jiangxi Province (20204BCJ22015 and 20202ACBL203001) and the Jiangxi Provincial Key Laboratory of Functional Molecular Materials Chemistry (20212BCD42018).

References

1 X. Qin, X. Liu, W. Huang, M. Bettinelli and X. Liu, Lanthanide-activated phosphors based on 4f-5d optical transitions: theoretical and experimental aspects, *Chem. Rev.*, 2017, **117**, 4488–4527.

2 D. C. Mukunda, J. Rodrigues, V. K. Joshi, C. R. Raghushaker and K. K. Mahato, A comprehensive review on LED-induced fluorescence in diagnostic pathology, *Biosens. Bioelectron.*, 2022, 114230.

3 Z. Zeng, M. Sun, S. Zhang, H. Zhang, X. Shi, S. Ye, B. Huang, Y. Du and C. H. Yan, Rare–Earth–Based Perovskite $Cs_2AgScCl_6$: Bi for Strong Full Visible Spectrum Emission, *Adv. Funct. Mater.*, 2022, **32**, 2204780.

4 Z. Wang, Y. Zhang, C. Wang, X. Zheng, Y. Zheng, L. Gao, C. Yang, Y. Li, L. Qu and Y. Zhao, Color–tunable polymeric long–persistent luminescence based on polyphosphazenes, *Adv. Mater.*, 2020, **32**, 1907355.

5 J.-X. Wang, C. Li and H. Tian, Energy manipulation and metal-assisted photochromism in photochromic metal complex, *Coord. Chem. Rev.*, 2021, **427**, 213579.

6 M. K. Hossain, S. Hossain, M. H. Ahmed, M. I. Khan, N. Haque and G. A. Raihan, A review on optical applications, prospects, and challenges of rare-earth oxides, *ACS Appl. Electron. Mater.*, 2021, **3**, 3715–3746.

7 A. A. Koegel, E. M. Mozur, I. W. Oswald, N. H. Jalarvo, T. R. Prisk, M. Tyagi and J. R. Neilson, Correlating broadband photoluminescence with structural dynamics in layered hybrid halide perovskites, *J. Am. Chem. Soc.*, 2022, **144**, 1313–1322.

8 C. Pareja-Rivera, J. A. Morán-Muñoz, A. P. Gómora-Figueroa, V. Jancik, B. Vargas, J. Rodríguez-Hernández and D. Solis-Ibarra, Optimizing Broadband Emission in 2D Halide Perovskites, *Chem. Mater.*, 2022, **34**, 9344–9349.

9 N. Dehnhardt, J. N. Luy, P. Klement, L. Schipplick, S. Chatterjee, R. Tonner and J. Heine, Mixed Group 14–15 Metalates as Model Compounds for Doped Lead Halide Perovskites, *Angew. Chem., Int. Ed.*, 2021, **60**, 3906–3911.

10 L. Mao, P. Guo, M. Kepenekian, I. Hadar, C. Katan, J. Even, R. D. Schaller, C. C. Stoumpos and M. G. Kanatzidis, Structural diversity in white-light-emitting hybrid lead

bromide perovskites, *J. Am. Chem. Soc.*, 2018, **140**, 13078–13088.

11 C. Q. Jing, J. Wang, H. F. Zhao, W. X. Chu, Y. Yuan, Z. Wang, M. F. Han, T. Xu, J. Q. Zhao and X. W. Lei, Improving Broadband White–Light Emission Performances of 2D Perovskites by Subtly Regulating Organic Cations, *Chem. – Eur. J.*, 2020, **26**, 10307–10313.

12 C. Sun, J.-P. Zang, Y.-Q. Liu, Q.-Q. Zhong, X.-X. Xing, J.-P. Li, C.-Y. Yue and X.-W. Lei, Lead-free hybrid indium perovskites with highly efficient and stable green light emissions, *CCS Chem.*, 2022, **4**, 3106–3121.

13 L. Zhou, J. F. Liao, Z. G. Huang, J. H. Wei, X. D. Wang, W. G. Li, H. Y. Chen, D. B. Kuang and C. Y. Su, A highly red–emissive lead–free indium–based perovskite single crystal for sensitive water detection, *Angew. Chem.*, 2019, **131**, 5331–5335.

14 Y. Wu, C.-M. Shi, S.-R. Kang and L.-J. Xu, Antimony-doped indium-based halide single crystals enabling white-light emission, *Inorg. Chem. Front.*, 2022, **9**, 5008–5015.

15 Y.-Y. Ma, H.-Q. Fu, X.-L. Liu, Y.-M. Sun, Q.-Q. Zhong, W.-J. Xu, X.-W. Lei, G.-D. Liu and C.-Y. Yue, Zero-Dimensional Organic–Inorganic Hybrid Indium Chlorides with Intrinsic Blue Light Emissions, *Inorg. Chem.*, 2022, **61**, 8977–8981.

16 D. Chen, S. Hao, G. Zhou, C. Deng, Q. Liu, S. Ma, C. Wolverton, J. Zhao and Z. Xia, Lead-free broadband orange-emitting zero-dimensional hybrid $(PMA)_3InBr_6$ with direct band gap, *Inorg. Chem.*, 2019, **58**, 15602–15609.

17 N. Sun, J. Lin, S. He, J. Cao, Z. Guo, J. Zhao, Q. Liu and W. Yuan, High-Efficiency Intrinsic Yellow-Orange Emission in Hybrid Indium Bromide with Double Octahedral Configuration, *Inorg. Chem.*, 2023, **62**, 3018–3025.

18 J. Lin, Z. Guo, K. Liu, N. Sun, J. Cao, X. Chen, J. Zhao, Q. Liu and W. Yuan, Tunable Bright White Light Emission with Ultra–High Color Rendering Index Induced by Trigonal Bipyramid Unit, *Adv. Opt. Mater.*, 2023, **11**, 2202304.

19 S. Feng, Y. Ma, S. Wang, S. Gao, Q. Huang, H. Zhen, D. Yan, Q. Ling and Z. Lin, Light/Force–Sensitive 0D Lead–Free Perovskites: From Highly Efficient Blue Afterglow to White Phosphorescence with Near–Unity Quantum Efficiency, *Angew. Chem.*, 2022, **134**, e202116511.

20 P. Han, C. Luo, S. Yang, Y. Yang, W. Deng and K. Han, All–inorganic lead–free 0D perovskites by a doping strategy to achieve a PLQY boost from < 2% to 90%, *Angew. Chem.*, 2020, **132**, 12809–12813.

21 T. Jun, K. Sim, S. Iimura, M. Sasase, H. Kamioka, J. Kim and H. Hosono, Lead–free highly efficient blue–emitting $Cs_3Cu_2I_5$ with 0D electronic structure, *Adv. Mater.*, 2018, **30**, 1804547.

22 M. B. Gray, S. Hariyani, T. A. Strom, J. D. Majher, J. Brgoch and P. M. Woodward, High-efficiency blue photoluminescence in the $Cs_2NaInCl_6$: Sb^{3+} double perovskite phosphor, *J. Mater. Chem. C*, 2020, **8**, 6797–6803.

23 C. Sun, Z. Deng, Z. Li, Z. Chen, X. Zhang, J. Chen, H. Lu, P. Canepa, R. Chen and L. Mao, Achieving Near–unity Photoluminescence Quantum Yields in Organic–Inorganic Hybrid Antimony(III) Chlorides with the $[SbCl_5]$ Geometry, *Angew. Chem., Int. Ed.*, 2023, **62**, e202216720.

24 C. W. Tang, S. A. VanSlyke and C. H. Chen, Electroluminescence of doped organic thin films, *J. Appl. Phys.*, 1989, **65**, 3610–3616.

25 J.-H. Wei, J.-F. Liao, L. Zhou, J.-B. Luo, X.-D. Wang and D.-B. Kuang, Indium-antimony-halide single crystals for high-efficiency white-light emission and anti-counterfeiting, *Sci. Adv.*, 2021, **7**, eabg3989.

26 C. Zhou, H. Lin, Y. Tian, Z. Yuan, R. Clark, B. Chen, L. J. van de Burgt, J. C. Wang, Y. Zhou and K. Hanson, Luminescent zero-dimensional organic metal halide hybrids with near-unity quantum efficiency, *Chem. Sci.*, 2018, **9**, 586–593.

27 L. Mao, Y. Wu, C. C. Stoumpos, B. Traore, C. Katan, J. Even, M. R. Wasielewski and M. G. Kanatzidis, Tunable White-Light Emission in Single-Cation-Templated Three-Layered 2D Perovskites $(CH_3CH_2NH_3)_4Pb_3Br_{10-x}Cl_x$, *J. Am. Chem. Soc.*, 2017, **139**, 11956–11963.

28 Y. Li, C. Ji, L. Li, S. Wang, S. Han, Y. Peng, S. Zhang and J. Luo, (γ-Methoxy propyl amine)$_2$PbBr$_4$: a novel two-dimensional halide hybrid perovskite with efficient bluish white-light emission, *Inorg. Chem. Front.*, 2021, **8**, 2119–2124.

29 L. Kang and Z. Lin, Regulation strategy of white emission from organic-inorganic hybrid metal halide perovskites, *Inorg. Chem. Front.*, 2022, **10**, 13–36.

30 Q. Ran, Y. Zhang, J. Yang, R. He, L. Zhou and S. Hu, White-light defect emission and enhanced photoluminescence efficiency in a 0D indium-based metal halide, *J. Mater. Chem. C*, 2022, **10**, 1999–2007.

31 Z. Li, Y. Li, P. Liang, T. Zhou, L. Wang and R.-J. Xie, Dual-band luminescent lead-free antimony chloride halides with near-unity photoluminescence quantum efficiency, *Chem. Mater.*, 2019, **31**, 9363–9371.

32 L. Mao, Y. Wu, C. C. Stoumpos, M. R. Wasielewski and M. G. Kanatzidis, White-light emission and structural distortion in new corrugated two-dimensional lead bromide perovskites, *J. Am. Chem. Soc.*, 2017, **139**, 5210–5215.

33 Z. Qi, H. Gao, X. Yang, Y. Chen, F.-Q. Zhang, M. Qu, S.-L. Li and X.-M. Zhang, A One-Dimensional Broadband Emissive Hybrid Lead Iodide with Face-Sharing PbI_6 Octahedral Chains, *Inorg. Chem.*, 2021, **60**, 15136–15140.

34 Z. Qi, Y. Chen, Y. Guo, X. Yang, H. Gao, G. Zhou, S.-L. Li and X.-M. Zhang, Highly efficient self-trapped exciton emission in a one-dimensional face-shared hybrid lead bromide, *Chem. Commun.*, 2021, **57**, 2495–2498.

35 R. Gautier, M. Paris and F. Massuyeau, Exciton self-trapping in hybrid lead halides: role of halogen, *J. Am. Chem. Soc.*, 2019, **141**, 12619–12623.

36 Z. Yuan, C. Zhou, Y. Tian, Y. Shu, J. Messier, J. C. Wang, L. J. Van De Burgt, K. Kountouriotis, Y. Xin and E. Holt, One-dimensional organic lead halide perovskites with efficient bluish white-light emission, *Nat. Commun.*, 2017, **8**, 14051.

37 K. Dave, W.-T. Huang, T. Leśniewski, A. Lazarowska, D. Jankowski, S. Mahlik and R.-S. Liu, Photoluminescence enhancement study in a Bi-doped $Cs_2AgInCl_6$ double per-

ovskite by pressure and temperature-dependent self-trapped exciton emission, *Dalton Trans.*, 2022, **51**, 2026–2032.

38 S. Wang, Y. Yao, Z. Wu, Y. Peng, L. Li and J. Luo, Realization of "warm" white light via halide substitution in polar two-dimensional hybrid perovskites (2meptH$_2$)PbCl$_x$, Br$_{4-x}$, *J. Mater. Chem. C*, 2018, **6**, 12267–12272.

39 X. Cheng, S. Yue, R. Chen, J. Yin and B.-B. Cui, White Light-Emitting Diodes Based on One-Dimensional Organic–Inorganic Hybrid Metal Chloride with Dual Emission, *Inorg. Chem.*, 2022, **61**, 15475–15483.

40 S. Elleuch, A. Lusson, S. Pillet, K. Boukheddaden and Y. Abid, White light emission from a zero-dimensional lead chloride hybrid material, *ACS Photonics*, 2020, **7**, 1178–1187.

41 J. Cao, J. Lin, K. Liu, Y. Xiong, N. Wang, S. He, X. Zhang, Z. Guo, X. Chen and J. Zhao, Antimony and bismuth cooperation to enhance the broad yellow photoluminescence of zero-dimensional hybrid halide, *J. Mater. Chem. C*, 2022, **10**, 9841–9848.

42 J. Alonso, M. Martinez-Lope, M. Casais and M. Fernandez-Diaz, Evolution of the Jahn– Teller distortion of MnO$_6$ octahedra in RMnO3 perovskites (R = Pr, Nd, Dy, Tb, Ho, Er, Y): a neutron diffraction study, *Inorg. Chem.*, 2000, **39**, 917–923.

43 J. Lin, Z. Guo, N. Sun, K. Liu, X. Chen, J. Zhao, Q. Liu and W. Yuan, High-efficiency red photoluminescence achieved by antimony doping in organic–inorganic halide (C$_{11}$H$_{24}$N$_2$)$_2$[InBr$_6$][InBr$_4$], *J. Mater. Chem. C*, 2022, **10**, 5905–5913.

44 Z. Wang and X. Huang, Luminescent Organic–Inorganic Hybrid Metal Halides: An Emerging Class of Stimuli–Responsive Materials, *Chem. – Eur. J.*, 2022, **28**, e202200609.

45 L. Zhou, J. F. Liao, Z. G. Huang, J. H. Wei, X. D. Wang, H. Y. Chen and D. B. Kuang, Intrinsic self–trapped emission in 0D lead–free (C$_4$H$_{14}$N$_2$)$_2$In$_2$Br$_{10}$ single crystal, *Angew. Chem.*, 2019, **131**, 15581–15586.

46 T. Cao, Y. Wang, Z. Xu, L. Ye and X. Zhuang, Two Zero–Dimensional In^{3+}–Based Hybrid Halides: Single–Component Materials Showing Bluish–White–Light Emission, *ChemistrySelect*, 2022, **7**, e202203074.

47 C. Chen, J. Xiang, Y. Chen, M. Jin, J. Zheng, N. Zhang and C. Guo, White-light emission lead-free perovskite phosphor Cs$_2$ZrCl$_6$: Sb^{3+}, *Ceram. Int.*, 2022, **48**, 1851–1856.

48 R. Zhang, X. Xu, X. Mao, Z. Wang, P. Wang, Y. Yang, J. Chen, R. Lu, W. Deng and K. Han, Excitation–Dependent Emission in All–Inorganic Lead–Free Cs$_2$ScCl$_5$·H$_2$O Perovskite Crystals, *Laser Photonics Rev.*, 2022, **16**, 2100689.

49 J. Zhou, X. Rong, M. S. Molokeev, Y. Wang, X. Yun, D. Xu and X. Li, Alloying Cs$^+$ into Rb$_2$ZrCl$_6$:Te^{4+} toward highly efficient and stable perovskite variants, *Mater. Chem. Front.*, 2021, **5**, 4997–5003.

50 Z. Gong, W. Zheng, P. Huang, X. Cheng, W. Zhang, M. Zhang, S. Han and X. Chen, Highly efficient Sb^{3+} emitters in 0D cesium indium chloride nanocrystals with switchable photoluminescence through water-triggered structural transformation, *Nano Today*, 2022, **44**, 101460.

51 H. Peng, Y. Tian, X. Wang, T. Huang, Z. Yu, Y. Zhao, T. Dong, J. Wang and B. Zou, Pure white emission with 91.9% photoluminescence quantum yield of [(C$_3$H$_7$)$_4$N]$_2$Cu$_2$I$_4$ out of polaronic states and ultra-high color rendering index, *ACS Appl. Mater. Interfaces*, 2022, **14**, 12395–12403.

52 Z.-Z. Zhang, J.-C. Jin, L.-K. Gong, Y.-P. Lin, K.-Z. Du and X.-Y. Huang, Co-luminescence in a zero-dimensional organic–inorganic hybrid antimony halide with multiple coordination units, *Dalton Trans.*, 2021, **50**, 3586–3592.

53 J. Luo, X. Wang, S. Li, J. Liu, Y. Guo, G. Niu, L. Yao, Y. Fu, L. Gao and Q. Dong, Efficient and stable emission of warm-white light from lead-free halide double perovskites, *Nature*, 2018, **563**, 541–545.

54 W. Zhang, J. Wei, Z. Gong, P. Huang, J. Xu, R. Li, S. Yu, X. Cheng, W. Zheng and X. Chen, Unveiling the Excited–State Dynamics of Mn^{2+} in 0D Cs$_4$PbCl$_6$ Perovskite Nanocrystals, *Adv. Sci.*, 2020, **7**, 2002210.

55 L.-K. Wu, H.-Y. Sun, L.-H. Li, R.-F. Li, H.-Y. Ye and J.-R. Li, Te^{4+}-Doping Rubidium Scandium Halide Perovskite Single Crystals Enabling Optical Thermometry, *J. Phys. Chem. C*, 2022, **126**, 21689–21698.

56 R. Zeng, K. Bai, Q. Wei, T. Chang, J. Yan, B. Ke, J. Huang, L. Wang, W. Zhou and S. Cao, Boosting triplet self-trapped exciton emission in Te(IV)-doped Cs$_2$SnCl$_6$ perovskite variants, *Nano Res.*, 2021, **14**, 1551–1558.

57 W. Stadler, D. Hofmann, H. Alt, T. Muschik, B. Meyer, E. Weigel, G. Müller-Vogt, M. Salk, E. Rupp and K. Benz, Optical investigations of defects in Cd$_{1-x}$Zn$_x$Te, *Phys. Rev. B: Condens. Matter Mater. Phys.*, 1995, **51**, 10619.

58 J. Krustok, H. Collan and K. Hjelt, Does the low-temperature Arrhenius plot of the photoluminescence intensity in CdTe point towards an erroneous activation energy?, *J. Appl. Phys.*, 1997, **81**, 1442–1445.

59 C. Sun, Q.-Q. Zhong, X. Zhang, P.-C. Xiao, Y. Cheng, Y.-J. Gao, G.-D. Liu and X.-W. Lei, A Zero-Dimensional Hybrid Cadmium Perovskite with Highly Efficient Orange–Red Light Emission, *Inorg. Chem.*, 2021, **60**, 18879–18888.

60 L. Zhou, J. F. Liao, Z. G. Huang, J. H. Wei, X. D. Wang, H. Y. Chen and D. B. Kuang, Intrinsic self–trapped emission in 0D lead–free (C$_4$H$_{14}$N$_2$)$_2$In$_2$Br$_{10}$ single crystal, *Angew. Chem.*, 2019, **131**, 15581–15586.

61 J. P. Perdew and M. Levy, Physical content of the exact Kohn-Sham orbital energies: band gaps and derivative discontinuities, *Phys. Rev. Lett.*, 1983, **51**, 1884.

62 R. Zhang, X. Mao, Y. Yang, S. Yang, W. Zhao, T. Wumaier, D. Wei, W. Deng and K. Han, Air–stable, lead–free zero–dimensional mixed bismuth–antimony perovskite single crystals with ultra–broadband emission, *Angew. Chem., Int. Ed.*, 2019, **58**, 2725–2729.

63 L. Zhou, J. F. Liao, Y. Qin, X. D. Wang, J. H. Wei, M. Li, D. B. Kuang and R. He, Activation of Self–Trapped Emission in Stable Bismuth–Halide Perovskite by Suppressing Strong Exciton–Phonon Coupling, *Adv. Funct. Mater.*, 2021, **31**, 2102654.